

Role of cellular tone and microenvironmental conditions on cytoskeleton stiffness assessed by tensegrity model

S. Wendling^{1,a}, E. Planus², V.M. Laurent², L. Barbe¹, A. Mary², C. Oddou¹, and D. Isabey²

¹ Laboratoire de Mécanique Physique, CNRS-ESA 7052, Université Paris 12-Val de Marne, 61 avenue du Général de Gaulle, 94010 Créteil Cedex, France

² INSERM, U492 Physiopathologie et Thérapeutique Respiratoires, Hôpital Henri Mondor, 94010 Créteil, France

Received: 1 July 1998 / Revised: 16 November 1998 / Accepted: 22 October 1999

Abstract. We have tried to understand the role of cellular tone (or internal tension mediated by actin filaments) and interactions with the microenvironment on cellular stiffness. For this purpose, we compared the apparent elasticity modulus of a 30-element tensegrity structure with cytoskeleton stiffness measured in subconfluent and confluent adherent cells by magnetocytometry, assessing the effect of changing cellular tone by treatment with cytochalasin D. Intracellular and extracellular mechanical interactions were analyzed on the basis of the non-dimensional relationships between the apparent elasticity modulus of the tensegrity structure normalized by Young's modulus of the elastic element *versus*: (i) element size, (ii) internal tension, and (iii) number of spatially fixed nodes, for small deformation conditions. Theoretical results and rigidity measurements in adherent cells consistently showed that higher cellular tone and stronger interdependencies with cellular environment tend to increase cytoskeleton stiffness. Visualization of the actin lattice before and after depolymerization by cytochalasin D tended to confirm the geometrical and mechanical assumptions supported by analysis of the present model.

PACS. 87.17.Aa Theory and modeling; computer simulation – 87.16.Ka Filaments, microtubules, their networks, and supramolecular assemblies – 45.10.Na Geometrical and tensorial methods

1 Introduction

A large number of *in vivo* and *in vitro* studies have shown that mechanical interactions between cells and the cellular environment play a fundamental role in biological processes such as migration, growth and morphogenesis [1–3]. For instance, interactions between cell surface adhesion receptors and components of the extracellular matrix (ECM) govern cell migration [4]. Moreover, a recent study by our group [5] showed that, during the process of epithelial wound repair, cell adhesion and cellular stiffness were both decreased in order to promote cell migration. It is noteworthy that cellular stiffness is also related to the mechanical properties of the cytoskeletal network constituted by interconnected filamentous polymers [6]. For instance, tension generated by actin filaments provides the cellular tone, *i.e.* the cytoskeleton (CSK) internal tension. Pourati *et al.* (1998) have evidenced that the preexisting mechanical tension in CSK is a major determinant of cell deformability, as the higher the internal tension, the stiffer the endothelial cell [7]. Cell migration appears to result from tension forces generated by CSK filaments at sites of adhesion and depends on the ability of adhesion re-

ceptors (integrins) to simultaneously bind extracellular matrix components to CSK elements [4,8]. Although intracellular and extracellular factors are known to affect the mechanical behavior of the cells, the interdependencies between these factors and the mechanical response of the cell have not been fully elucidated, *e.g.* the relationship between cellular tone and stiffness remains largely unknown. Comprehensive models are therefore needed to relate the measured cytoskeleton stiffness to (i) internal tension and (ii) cell environmental conditions. However, amongst the various theoretical models previously proposed to describe the mechanical properties of living cells: foam models [9], rheological models [10–12] and, more recently, tensegrity models [13, 14], only the latter explicitly take into account internal tension, as only tensegrity models involve individual compressive and tensile elements which carry non-zero internal tension in the absence of external stress, as well as interrelations with the environment *via* discrete points [15]. The system constituted by the CSK together with both the focal adhesion complex and the ECM, has already been qualitatively described in terms of tensegrity architecture [16]. By analogy, in living cells anchored to the extracellular matrix, tension of the actin lattice would be balanced by the compression in microtubules associated with intermediate filaments and extracellular

^a e-mail: wendling@univ-paris12.fr

matrix (ECM), thus promoting internal tension, experimental evidence of which has been reported by many authors [17–20].

In this study, we have numerically solved the constitutive mechanical equations of a simplified 30-element tensegrity structure in order to describe the role of the main parameters governing the mechanical behavior of the overall structure, *i.e.* the physical element properties as well as the internal and environmental conditions such as internal tension and the number of fixed nodes. A large scale physical model of the same tensegrity structure was used to test the validity of the numerical resolution method. The previous study performed by Stamenovic *et al.* (1996) on a similar tensegrity structure has already reported the effects of internal and external stresses on the mechanical response of the structure with, however, a different theoretical approach and different characteristic parameters compared to the present study. The mechanical behavior of our theoretical model was compared to the behavior of cultured cells in which we attempted to specifically modify the tone and environmental conditions. The biological model elaborated for this comparison consisted in analyzing both the mechanical response and the actin filament distribution of adherent cells in which changes in intracellular conditions were obtained by cytochalasin D treatment, whereas changes in extracellular conditions were obtained by confluent and subconfluent states of growth.

2 Methods

2.1 Theoretical and physical tensegrity models

2.1.1 Characteristics of the 30-element tensegrity structure at reference state

The spatial tensegrity structure studied comprises six rigid elements (bars) compressed by twenty-four pre-stretched hyperelastic elements (cables), (see Fig. 1a). The cables and bars are defined, respectively, by their geometry, *i.e.* length l_c , radius r_c , cross-sectional area $S_c (= \pi r_c^2)$ (and l_b , r_b , $S_b (= \pi r_b^2)$), and mechanical properties, *i.e.* Young's modulus E_c (and E_b). T_c is the stretching force in cables and T_b is the compressing force in bars. The radius and Young's modulus of both elements and the length of the bars are considered to be constant, as the bars are supposed to be rigid.

At reference state (*i.e.* in the absence of applied external forces), the geometrical symmetry of the structure, in which the bars are aligned in pairs in three perpendicular planes of space, implies the following relationship between length of the bars l_b and length of the cables l_c , (exponent (r) means reference state) [21]:

$$\frac{l_c^{(r)}}{l_b} = \sqrt{3/8}. \quad (1)$$

At reference state, the stable shape of the tensegrity structure studied corresponds to the equilibrium between tension in the cables T_c and compression in the bars T_b ,

leading to the following relationship, which is independent of equation (1) [22]:

$$\frac{T_c^{(r)}}{T_b^{(r)}} = 0.408. \quad (2)$$

2.1.2 Node-attachment conditions and force applied to the 30-element tensegrity structure

The 30-element tensegrity model was always anchored to the substratum by spherical joints at the three inferior nodes $\{1, 2, 3\}$ and tested for a variable number of additional nodes, with a spatially fixed reference position. External forces were applied to the nodes $\{10, 11, 12\}$, which formed the superior plane which was parallel to the inferior plane $\{1, 2, 3\}$ at reference state (Fig. 1b). The rectangular base $\{\mathbf{i}, \mathbf{j}, \mathbf{k}\}$ constituted the referential system. External forces were applied either parallel to the k -axis (compression and extension forces) or parallel to the $\{\mathbf{i}, \mathbf{j}\}$ plane (shearing force). Only first order displacements in the directions of applied forces were considered for both small and large deformations. The so-called “overall displacement” of the structure was calculated from the relative displacement ΔL_k between the superior and inferior planes, which remained parallel for small deformations. For the large deformations studied here, for comparison with experimental results in a physical model, the position of the superior plane was calculated from the mean position of the three superior nodes. Second-order displacements, occurring with large deformations, particularly with shearing forces, were not considered in this study. Displacements of free nodes $\{10, 11, 12\}$ uniquely considered in the direction of external forces, constituted the unknown variables of the problem.

2.1.3 Constitutive equations of the theoretical tensegrity model

When an external force is applied, a new equilibrium state of the “structure-substratum” tensegrity system is reached. This equilibrium is obtained by resolving a system of equations expressing, at each node, the balance of forces between the various elements, taking into account the compatibility between nodal displacements and deformation of the elements. This equation system can be expressed by using a standard matrix displacement method summarized by:

$$\{\mathbf{F}\} = [\mathbf{K}]\{\mathbf{u}\}. \quad (3)$$

Equation (3) relates the vector of external forces $\{\mathbf{F}\}$ to the vector of elementary nodal displacements $\{\mathbf{u}\}$. The vector $\{\mathbf{F}\}$ is a 1×36 -column vector whose components are the three-dimensional components of forces applied to the twelve nodes. $[\mathbf{K}]$ is the global rigidity matrix of the structure (dimensions: 36×36) which involves the rigidity matrices $[\mathbf{K}]_p$ of a given constitutive element “p” (bar or cable). Similarly, the vector of nodal displacements $\{\mathbf{u}\}$ is

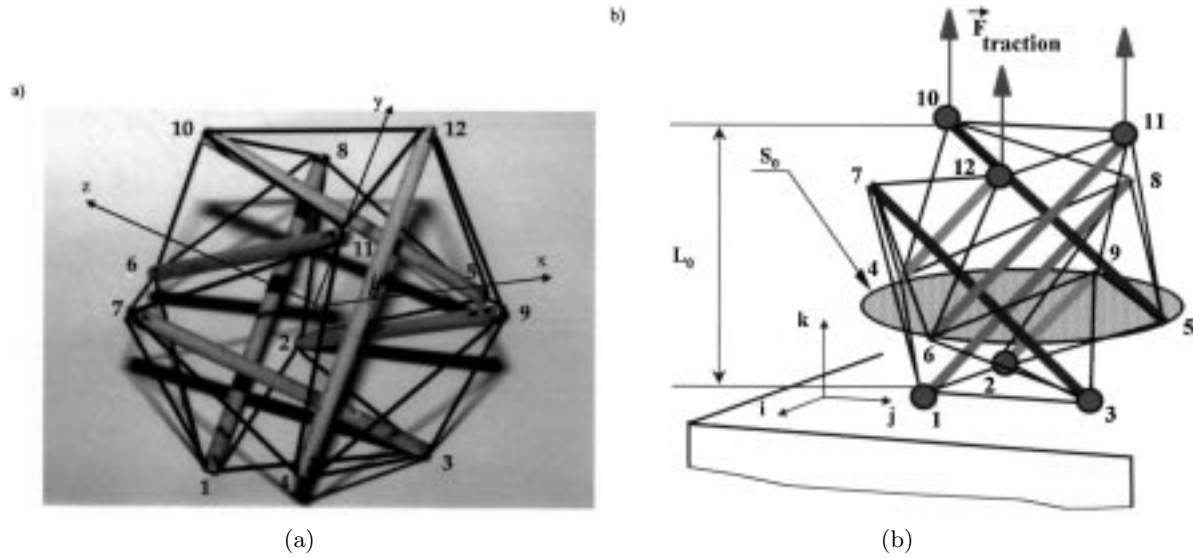


Fig. 1. Spatial view of the tensegrity structure studied (6 bars and 24 elastic cables). At reference state (no external forces applied to the structure), the 3 nodes {1, 2, 3} which defined the “inferior plane”, are anchored to a rigid and planar base. External forces are applied at nodal points {10, 11, 12} which define the “superior plane”, which remains parallel to the “inferior plane” in both experimental and numerical conditions during small deformation conditions. The rectangular base {*i*, *j*, *k*} is the referential system. External forces are applied either parallel to the *k*-axis (compression and extension forces) or parallel to the plane {*i*, *j*} (shear forces). Only first-order displacements in the directions of applied forces are considered. Second-order displacements, occurring at large deformation notably in shear, are not considered in this study. The overall strain resulting from application of external forces, is calculated using a reference length L_0 defined as the distance between the inferior and the superior planes of the structure at the reference state. To calculate the stress, we use a reference circular area S_0 , limiting the structure, *i.e.*, the 3 nodes {4, 5, 6} of the intermediate plane.

a 1×36 -column vector. According to the method proposed by Argyris and Scharpf [23], the rigidity matrix $[\mathbf{K}]_p$ for any given element p is defined by the sum of (i) the elastic rigidity matrix $[\mathbf{K}_E]_p$, which depends on the physical characteristics of the element and the coordinates of the nodes, and (ii) the geometric rigidity matrix $[\mathbf{K}_G]_p$, which depends on the actual stretching forces of the elements and the nodal coordinates.

$$[\mathbf{K}]_p = \begin{bmatrix} \frac{E_p \cdot S_p - T_p}{l_p} c_x^2 + \frac{T_p}{l_p}; & \bullet & \text{symmetrical} \\ \frac{E_p \cdot S_p - T_p}{l_p} c_x \cdot c_y & \frac{E_p \cdot S_p - T_p}{l_p} c_y^2 + \frac{T_p}{l_p}; & \bullet \\ \frac{E_p \cdot S_p - T_p}{l_p} c_x \cdot c_y & \frac{E_p \cdot S_p - T_p}{l_p} c_y \cdot c_z & \frac{E_p \cdot S_p - T_p}{l_p} c_z^2 + \frac{T_p}{l_p} \end{bmatrix}. \quad (4)$$

Note that the matrix $[\mathbf{K}]$ depends exclusively on the geometrical and mechanical properties of the bars and cables. Also note that (E_p, S_p) represents the elastic recoil force in each type of element and E_b, S_b must be much larger than E_c, S_c for rigid bars and hyperelastic cables.

2.1.4 Definition of the tensegrity structure rigidity

We analyzed the model response in terms of apparent elasticity modulus deduced from the stress-strain relationship. An apparent stress σ was defined by the ratio between

the norm of the external force vector and the mean cross-sectional area S_0 of the overall structure:

$$\sigma = \frac{\|\{\mathbf{F}\}\|}{S_0}. \quad (5)$$

S_0 corresponds to the circular area bounded by the 3 nodes {4, 5, 6} located in the intermediate plane of the structure at reference state (Fig. 1b). The radius of this characteristic circle is $R_0 = \left(\sqrt{0.875} \cdot \frac{\sqrt{3}}{3}\right) \cdot l_b$. By definition, S_0 depends on reference conditions and remains constant during deformation. Thus σ depends on the magnitude of the force and a quantity inversely proportional to the square element length l_b .

An apparent strain ε of the overall structure was defined along the *k*-axis for uni-axial extension and compression as:

$$\varepsilon = \frac{\Delta L_k}{L_0} \quad (6)$$

where L_0 is the distance between the inferior plane and the superior plane at reference state (Fig. 1b):

$$L_0 = (\sqrt{3}/2) \cdot l_b. \quad (7)$$

The apparent elasticity modulus of the structure was defined by the stress/strain ratio at small deformation ($\varepsilon < 5\%$):

$$E_A = \sigma/\varepsilon. \quad (8)$$

This apparent elasticity modulus E_A depends on the rigidity matrix $[\mathbf{K}]$ (Eqs. (3–8)). Dimensional analysis of the equations (Eqs. (1–4)) reveals that only 3 pertinent parameters are necessary to describe overall stiffness: l_c , $(E_c S_c)$ and T_c . The apparent elasticity modulus of the model E_A therefore exclusively depends on these quantities, related to the physical properties of tensile elements:

$$E_A = f(l_c; (E_c S_c); T_c). \quad (9)$$

2.1.5 Non dimensional quantities

The cable length $l_c^{(r)}$, the pre-stretching force $T_c^{(r)}$ of the tensegrity structure at reference state, and the apparent elasticity modulus E_A (Eq. (9)) were normalized using 2 characteristic quantities, Young's modulus of the cable E_c and radius of the cable r_c . We therefore defined the following non-dimensional parameters in order to analyze the apparent elasticity modulus results of the tensegrity model at the cellular level:

$$L^* = \frac{l_c^{(r)}}{r_c} \quad (10)$$

$$T^* = \frac{T_c^{(r)}}{E_c S_c} \quad (11)$$

$$E_A^* = \frac{E_A}{E_c}. \quad (12)$$

Taking into account equations (10–12), it follows from equation (9) that:

$$E_A^* = f^*(L^*, T^*). \quad (13)$$

Note that, by definition (Eq. (10)), L^* characterizes the relative volume of the constitutive elements, whereas T^* characterizes the strain of the hyperelastic cables at reference state.

2.1.6 Numerical resolution of the equilibrium force equations

The equation system (3) was resolved numerically by a linear incremental method. A constant incremental force was applied at each step and the new spatial position of the nodes was calculated from the final nodal position determined at the previous step. The pre-stretching forces in the elements of the deformed tensegrity structure were calculated by considering the lengthening or shortening of the elements and their constant physical properties (Young's modulus E_p ; cross-sectional area S_p ; resting length l_{0p}). The deformed shape of the structure at a given applied force was deduced from the difference between the referential and last positions of the nodes. When studying small deformations of the structure, we only considered displacement of the three superior nodes in the direction of loading, and therefore ignored nodal displacements in other directions.

2.1.7 Experimental investigation of physical tensegrity structures

Deformation of physical models (Fig. 1a) was determined experimentally by using a traction-compression device which measured, by means of variable resistance gauges, the elastic forces under almost static controlled displacement (Adamel-Lhomargy). The 30-element tensegrity structure was placed in the traction-compression device so that the three basal nodes {1, 2, 3} were attached to the rigid, fixed base of the machine and constant displacement was applied to the three superior nodes {10, 11, 12}. The structure was extended and/or compressed depending on the direction of displacement. During shear, the three nodes of the superior plane {10, 11, 12} remained in the same plane, always parallel to the inferior plane described by the three basal nodes {1, 2, 3}. The rate of displacement was 0.015 m/s and the maximum resistant force measured was about 10 daN \pm 0.5%. Displacement and force were digitized, then analyzed on the computer using an acquisition/signal-analysis system (AcqknowledgeIII®, BIOPAC Inc., CA USA). Four different types of physical 30-element tensegrity structures were built by changing (i) the length of the compressive elements ($l_b = 100$ mm and $l_b = 150$ mm) and (ii) the extension of the hyperelastic cables ($T^* = 0.3$ and $T^* = 0.6$) at reference state. Bars were made from 1 meter wooden rods, 10 mm in diameter, and cables were made from a nitril rope, 2 mm in diameter. Young's modulus of the elements was determined by using the traction-compression device and was considered to be equal to 2500 MPa for bars, while the mean Young's modulus was considered to be equal to 5 MPa for cables.

2.2 Biological model

2.2.1 Cell culture

A549 human alveolar epithelial cells (American Type Culture Collection, Rockville, MD) were grown in DMEM containing 10% FBS, 2 mM L-glutamine, 50 IU/ml of penicillin, and 50 μ g/ml of streptomycin, and were incubated in a 5% CO₂-95% air atmosphere at 37 °C. Routine subcultures (passages 88 to 91) were performed at 1/20 split ratios by incubation with 0.025% trypsin-0.02% EDTA in calcium-and-magnesium-free PBS for 10 minutes at 37 °C.

2.2.2 Cytoskeleton stiffness measured by magnetocytometry

Cytoskeleton (CSK) stiffness was assessed by magnetocytometry (MTC) using a device developed in the laboratory [24], similar to that previously described by Wang *et al.* [25,26]. The technique uses RGD-coated ferromagnetic microbeads in combination with a magnetic twisting device which allows application of a magnetic torque directly to the cell surface by microbeads linked to integrins and hence to the CSK [27]. Microbeads were firstly magnetized using a 0.15 tesla magnetic pulse (150 μ s). The

magnetic torque was then generated by applying a perpendicular uniform magnetic field created by Helmholtz coils (≤ 5 mT). The torque was calibrated from beads rotating in fluids of known viscosity under predetermined uniform magnetic fields [28]. Similarly, an estimated characteristic stress applied to the CSK was deduced according to the method described by Wang *et al.* [26] from the torque to bead volume ratio. Strain was estimated from the degree of bead rotation measured by an on-line magnetometer. The magnitude of the resulting permanent field (2 to 3 beads per cell) was a few nanoTesla and remained almost constant over the duration of the twist application (≈ 1 min). CSK stiffness was then determined from the stress/strain ratio and analyzed for different levels of applied stress.

Bacteriologic dishes (96-well) were coated with $5 \mu\text{g}/\text{cm}^2$ of fibronectin for 3 hours at room temperature. Confluent cells were plated at a density of $50 \times 10^3/\text{well}$ ($30 \times 10^3/\text{well}$ for subconfluent cells) in complete medium with serum, 24 hours before experiments. Cells were incubated in serum-free medium with 1% BSA for 30 minutes before experiments.

Carboxyl ferromagnetic beads (4.5 μm in diameter, Spherotec Inc., IL USA) were coated with arginine-glycine-aspartic acid (RGD) peptide according to the manufacturer's instructions (Telios Pharmaceuticals Inc., CA USA). Before use, coated beads were incubated in serum-free medium supplemented with 1% BSA for at least 30 minutes at 37 °C to block non-specific binding. Beads were then added to the cells (40 μg per well) for 30 minutes at 37 °C in a 5% CO_2 -95% air incubator. Unbound beads were washed away with serum-free medium-1% BSA. Each cell culture well, with confluent or subconfluent cells, either untreated or treated with 1 $\mu\text{g}/\text{ml}$ of cytochalasin D for 20 min, was placed in the magnetocytometer to measure cytoskeleton stiffness for different levels of stress. Measurements were performed for 3 wells of the same culture and a given set of the conditions described above. Stiffness values and standard error therefore represent the mean of 3 separate magnetocytometric measurements under a given set of biological conditions.

2.2.3 Staining of F-actin with fluorescent phalloidin and confocal microscopy

Small plastic wells were fixed with silicone on round glass coverslips which were placed in Petri dishes and the inside surface of the wells (0.5 cm^2) was coated with fibronectin at a concentration of $5 \mu\text{g}/\text{cm}^2$. Cells were plated and treated with cytochalasin D under the same conditions as those described above. Cell monolayers were rinsed twice with warm cytoskeleton (CSK) buffer, 25 mM HEPES, 2 mM MgCl_2 , 30 mM MES, 10 mM EGTA, 300 mM sucrose, pH 6.9, in order to maintain CSK integrity, as previously described [29]. Cells were then fixed in 1% glutaraldehyde in CSK buffer for 15 minutes and incubated an additional 2 min with 0.5% Triton X100 and 0.25% glutaraldehyde in CSK buffer at 37 °C. The samples were rinsed twice with CSK buffer. 0.76 μM rhodaminated phalloidin was dissolved in CSK buffer and added

to each sample for 30 minutes in the dark and under a humid chamber at room temperature. Coverslips were rinsed twice for 5 minutes with CSK buffer, followed by a final rinse with ddH_2O . The coverslips were mounted with 100 μl of mounting medium on top of the cell monolayer to keep the cell thickness intact.

Samples were stored overnight at 4 °C before examination by laser confocal microscopy using an LSM 410 inverse phase microscope (Zeiss, Rueil-Malmaison, France), composed of two internal helium-neon lasers and one external argon ion laser. Image processing was performed using LSM 410 software. Cell fields were randomly selected, brought into focus using a x63/1.25 numerical aperture Plan Neofluar objective under transmitted light bright field conditions and briefly examined. A cross-sectional image was recorded under confocal conditions and used to establish a plane of focus above the glass surface. Optical sections were recorded every 1 μm to reveal intracellular fluorescence.

3 Results

3.1 Experimental and numerical stress-strain relationships in tensegrity models

Experimental results, expressed in terms of stress-strain relationship, were obtained from the analysis of four physical 30-element tensegrity structures with the three inferior nodes {1, 2, 3} anchored to the rigid base. These results were compared to the results of the numerical model in order to validate the linear incremental numerical method. For the two loading conditions tested, *i.e.* extension (Fig. 2a) and shear (Fig. 2c), the stress-strain relationships of these two models exhibited a similar non-linear behavior over a wide range of deformation ($\varepsilon = 90\%$), whereas they tended to diverge for the largest deformation values tested ($\varepsilon \geq 90\%$). For both theoretical and physical models, external forces were applied to the three superior nodes {10, 11, 12} and for elastic properties of the cables as constant as possible (see Method and Fig. 1b). When the strain of elastic cables at reference state was modified in a given physical structure ($T^* = 0.2, 0.5, 0.8$ in extension; $T^* = 0.05, 0.2, 0.6$ in shear), the stress-strain relationship of the overall structure was also modified, as the non-linearity of the curves became more marked as T^* increased (see Figs. 2b and 2d).

3.2 Local vs. global physical properties of the numerical tensegrity model

The normalized elasticity modulus E_A^* of the 30-element tensegrity structure was determined at small deformations ($\varepsilon \leq 5\%$) by numerical resolution of the constitutive equations and studied as a function of the two normalized quantities representative of (i) length L^* and (ii) mechanical properties T^* of the constitutive elements (see Eqs. (10, 11)), (Figs. 3 and 4). These numerical results corresponded to traction and compression and were obtained for a given attachment condition: three inferior nodes fixed

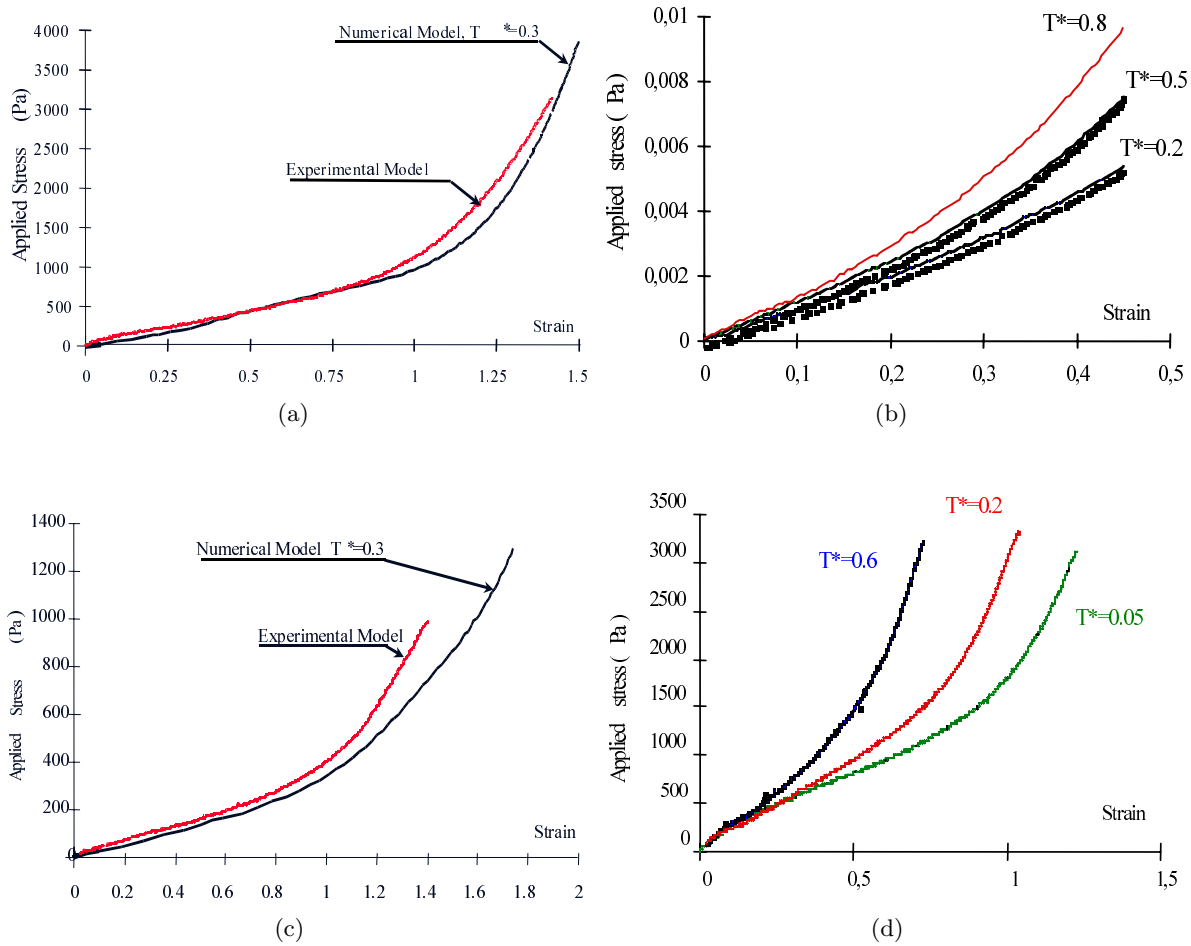


Fig. 2. Numerical and experimental results are expressed in terms of stress-strain relationships obtained in a given 30-element tensegrity structure (normalized tensile-element length $L^* = 61$) anchored to the base by means of the three inferior nodes $\{1, 2, 3\}$. Numerical and experimental results are compared when the structure is submitted to (i) uni-axial extension (Fig. 2a), and (ii) shear (Fig. 2c). Experimental error is within the limits of 5%. Discrepancies between experimental and numerical results are less than 5% for the range of strains tested $\varepsilon < 0.90$. The experimental stress-strain relationships are also compared for different levels of internal tension, characterized by various values of normalized elastic tension at reference state T^* ($= 0.2, 0.5, 0.8$ and $0.05, 0.2, 0.6$), and different types of loading (i) uni-axial extension (Fig. 2b) and (ii) shear (Fig. 2d). T^* is defined by the ratio between the pre-stretching force $T_c^{(r)}$ and the elastic recoil force ($E_c \cdot S_c$), considered to be constant. T^* also represents the persistent strain of the elastic element at the reference state. The 30-element tensegrity structure becomes stiffer, *i.e.* the slope of the stress-strain curve increases when internal tension, characterized by T^* , increases.

at the rigid base ($N = 3$). The $(E_A^* - L^*)$ relationships, obtained for three values of normalized elastic tension T^* , which differed by several orders of magnitude, exhibited L^{*-2} -dependence of the normalized elasticity modulus E_A^* over the entire range of L^* tested, as T^* was directly proportional to E_A^* (Fig. 3a). This L^{*-2} -dependence of E_A^* was not affected by the number of attachment points, while an additional number of spatially fixed nodes tended to increase the apparent elasticity modulus E_A^* (Fig. 3b). Quantitatively, from $N = 3$ to $N = 6$, the apparent elasticity modulus E_A^* was increased more than twofold, while from $N = 6$ to $N = 9$, E_A^* was not really modified.

The $(E_A^* - T^*)$ curves, obtained for three different attachment conditions and given values of L^* ($= 61$), exhibited a positive slope whose maximum value approached

$\sqrt{T^*}$ in the range $0.001 < T^* < 0.1$ (Fig. 4). This result demonstrates a property of the tensegrity model, *i.e.* a marked tendency to observe an increase in elasticity modulus E_A^* as the strain of elastic elements at reference state T^* increased. The dependence of T^* on the normalized apparent modulus E_A^* tended to decrease as the additional number of spatially fixed nodes increased from $N = 3$ to 6 (Fig. 4). By contrast, the $(E_A^* - T^*)$ relationships remained very similar from $N = 6$ to $N = 9$ (Fig. 4). It should be noted that reticulated networks are characterized by a much lower overall stiffness than the stiffness of the constitutive elements, *i.e.* E_A^* is always less than 1, because (i) the elements occupy a much smaller actual volume than the global volume of the structure, (ii) tensile and compressive elements are spatially rearranged under loading conditions.

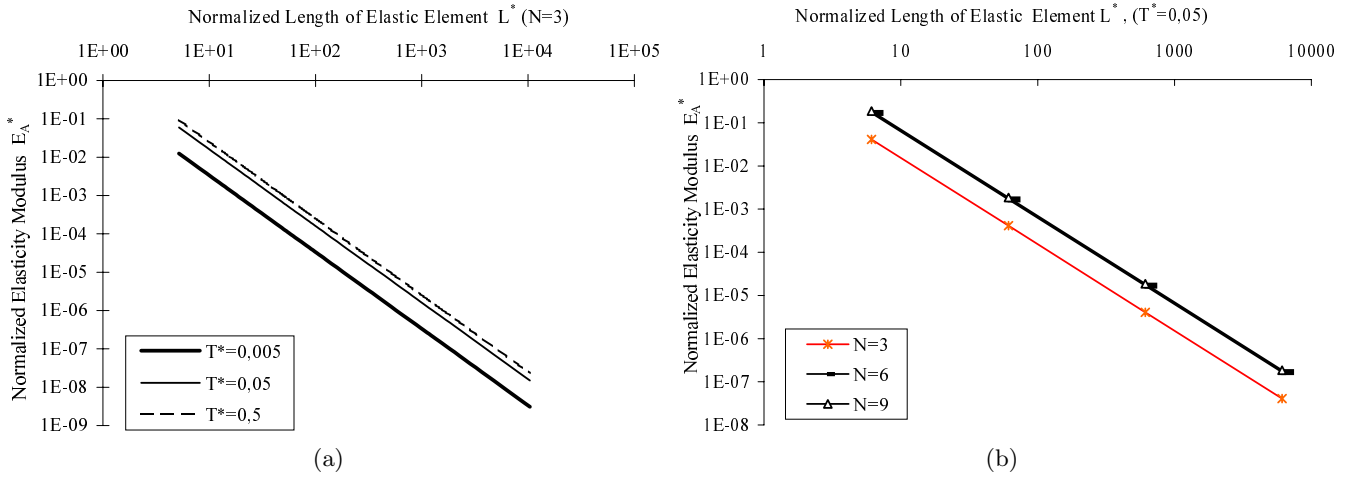


Fig. 3. Numerical results obtained for small deformations of the 30-element tensegrity structure anchored to the base by means of the three inferior nodes $\{1, 2, 3\}$ ($N = 3$). For extension and compression, the normalized apparent modulus E_A^* of the tensegrity structure is plotted against the normalized tensile-element length L^* :

(i) for three different values of normalized elastic tension at the reference state $T^*(= 0.005; 0.05; 0.5)$ in Figure 3a. The normalized apparent modulus E_A^* appears to be dependent on L^{*-2} for the two types of loading tested; L^* is defined by the ratio between the elastic element length $l_c^{(r)}$ (before loading) and the radius r_c of the elastic element, considered to be constant; (ii) for three different numbers of spatially fixed nodes and a given value of $T^*(= 0.05)$. $N = 3$ corresponds to the standard study conditions, $N = 6$ and $N = 9$ correspond to additional spatially fixed nodes, *i.e.*, those in the intermediate planes $\{4, 5, 6\}$ and $\{7, 8, 9\}$, respectively. The normalized apparent modulus E_A^* appeared to remain dependent on L^{*-2} for the 3 conditions of fixed nodes tested, but the apparent modulus increased E_A^* significantly from $N = 3$ to $N = 6$.

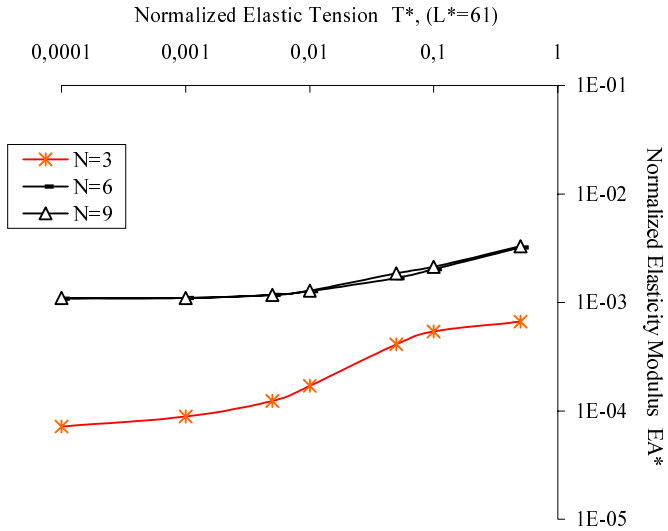


Fig. 4. Numerical results obtained for small deformation of the 30-element tensegrity structure anchored to the base by means of the three inferior nodes $\{1, 2, 3\}$ ($N = 3$). For extension and compression, the normalized apparent modulus E_A^* of the tensegrity structure is plotted against the normalized elastic tension T^* and a given value of $L^*(= 61)$. The normalized apparent modulus E_A^* appears to be at most dependent on $\sqrt{T^*}$ ($10^{-3} \leq T^* \leq 10^{-1}$), whereas the T^* -dependency is reduced below and above this T^* -range. The T^* -dependency on E_A^* is moderately decreased when the number of spatially fixed nodes is increased from $N = 3$ to $N = 6$ and remains unmodified from $N = 6$ to $N = 9$.

3.3 Tone and environmental effects on cultured cell stiffness and actin lattice distribution

Using magnetocytometry and confocal microscopy, the stiffness and actin lattice arrangement of cultured epithelial cells was evaluated under two controlled environmental conditions, *i.e.* subconfluence and confluence, and for two internal conditions of actin lattice distribution induced by the presence or absence of cytochalasin D (Fig. 5). For the two environmental conditions tested, addition of cytochalasin D notably reduced both the stiffness and the stiffening response (Fig. 5a). In both confluent and subconfluent adherent cells, the mean value of cell stiffness was decreased by more than one half, whereas the stiffening response was decreased by one third after treatment with cytochalasin D (Fig. 5a). The spatial distribution of actin filaments is presented in Figures 5b–5e, where actin filaments are shown in different colors depending on their height in the cell, *i.e.* from red (basal plane) to blue (apical plane). Subconfluent cells were widely distributed with a high density of actin filaments (F-actin) organized in stress fibers predominantly located in a thin ($2 \mu\text{m}$ thick) inferior layer (see red colored filaments in Fig. 5b). Note that stress fibers attached to focal adhesion points had a convex curved shape orientated towards the cell nucleus. Confluent cells had a rounder appearance with a marked contour of F-actin bundles, as spreading was limited by adjacent cells. F-actin bundles were distributed around the cell (Fig. 5c) in addition to the dense actin lattice located in a thin inferior layer. Disruption of F-actin fibers was visible after cytochalasin D treatment in both

subconfluent and confluent cells. Moderate cell retraction associated with a moderate increase in cell thickness were observed in subconfluent cells (Fig. 5d). In treated confluent cells, complete disorganization of the actin lattice was observed throughout the cell, resulting in a moderate increase in cell thickness (actin filaments appeared to be predominantly located at the intermediate level of the cell extending in the range of 3 to 9 μm from the basal plane (see yellow and green colored filaments in Fig. 5d) with loss of the marked contour of F-actin fibers (Fig. 5e).

4 Discussion

In this study, we used a 30-element tensegrity model, previously used as a structural model of the mechanical response of the cytoskeleton [13,14]. This model basically considers the discrete nature of the CSK structure in terms of interconnected filaments (actin lattice, microtubules and intermediate filament networks) and CSK interrelations with the cellular environment *via* focal adhesion points. However, this 30-element tensegrity model remains dramatically simplified compared to the complexity of the CSK architecture [30]. However, higher order structures studied by other authors [26,31] have revealed non-linear stress-strain relationships similar to those observed in Figure 2, suggesting that the results obtained in the 30-element tensegrity model could be representative of tensegrity structures in general. Nevertheless, this model has been shown to describe a number of features expressed by adherent cells during mechanical measurement. In this study, we investigated the relative contributions of scale, internal tension and number of spatially fixed nodes on the overall stiffness of this simplified tensegrity structure and compared these theoretical results to those obtained in adherent epithelial cells. Whether the cellular motion induced by magnetic bead rotation during MTC measurements represented a traction motion or a shearing motion is not of major importance in this study, as the biological results were compared to tensegrity model results which, at first sight, are quite similar in terms of shear (with or without slight rotation) and traction (Fig. 2).

Firstly, the present study demonstrates that a decrease in internal tension, induced in the model by a decrease in cable strain at reference state, is accompanied by a decrease in structural stiffness. Similarly, biological results showed that an alteration of internal tension, induced by disruption of the actin lattice after cytochalasin D treatment, resulted in a decrease in cellular stiffness in both confluent and subconfluent cells. Secondly, the tensegrity model predicts that increasing the number of spatially fixed nodes in order to mimic stronger cell-cell interdependencies results in increased structural stiffness. The biological results seem to indicate that confluence might contribute to cellular stiffness. The contribution of cell-cell attachment to cellular stiffness is suggested by the finding that round confluent cells have almost the same stiffness as spread subconfluent cells, despite their decreased attachment to the ECM. These results confirm that the 30-element tensegrity model could be used as a first

quantitative approach to estimate CSK tone from measured cellular stiffness and that environmental conditions affect cellular response in that stronger interdependencies with the cellular environment tend to increase cellular stiffness.

It should be emphasized that the non-dimensional results presented above apply to 30-element tensegrity structures which are very different from real cells in terms of size, mechanical properties of structural elements and attachment conditions, including the passage from microscale to macroscale. Moreover, the relative agreement between experimental and numerical results tends to confirm the validity of the theoretical method, up to the limit defined by the geometrical conditions of physical models, *e.g.* a characteristic length L^* , and/or an overall deformation ε avoiding contact between the bars. The underestimation of the numerical model, observed in the upper range of deformation (Figs. 2a and 2c), may be attributed to a more limited spatial mobility of the bars in the experimental model compared to the numerical model. This is especially true during shear, where the three nodes of the superior plane in the experimental model were constrained to remain in a plane strictly parallel to the inferior plane. It is interesting to note that, in the numerical model, shear forces applied to the three superior nodes $\{10, 11, 12\}$ resulted in a rotary shearing motion with a secondary order of magnitude compared to the main axial displacement. This secondary shearing motion was not permitted under experimental conditions, and probably contributed to the more marked non-linearity of the experimental stress-strain relationship for $\varepsilon \geq 90\%$ in Figures 2a and 2c.

4.1 Comparison with Stamenovic's results obtained in the same model

The present results, like those reported by Stamenovic, were obtained on the same 30-element tensegrity structure. They all show similar stress-stiffening responses to traction as well as a stiffening process associated with an increase in internal tension [13,32]. However, the analysis by Stamenovic *et al.* differed from our analysis: (i) they applied the principle of virtual work to 1/8 of the structure [13] and Euler's equations for buckling [14], while we applied the equilibrium force equations at each node, (ii) they only tested traction by stretching two parallel bars, while we studied traction, compression and shear for three nodes anchored to the rigid substratum and a variable number of additional spatially fixed nodes, (iii) they used a stiffness definition (rigidity coefficient $E = T/\Delta s_x$) which differs from the definition of an apparent elasticity modulus ($E_A = \sigma/\varepsilon$) used in our model. These discrepancies make it difficult to quantitatively compare stiffness results for both small and large deformation conditions [13,32]. It is interesting to note that, the prestress increase in structural stiffness was obtained for the same range of prestress values, *i.e.* the range of initial cable strain $\xi = [0-1]$ in Stamenovic's study corresponded to the range of normalized elastic tension $T^*(= \xi/(1-\xi)) = [0-\infty]$ observed in our study. Application of these results at the cellular level

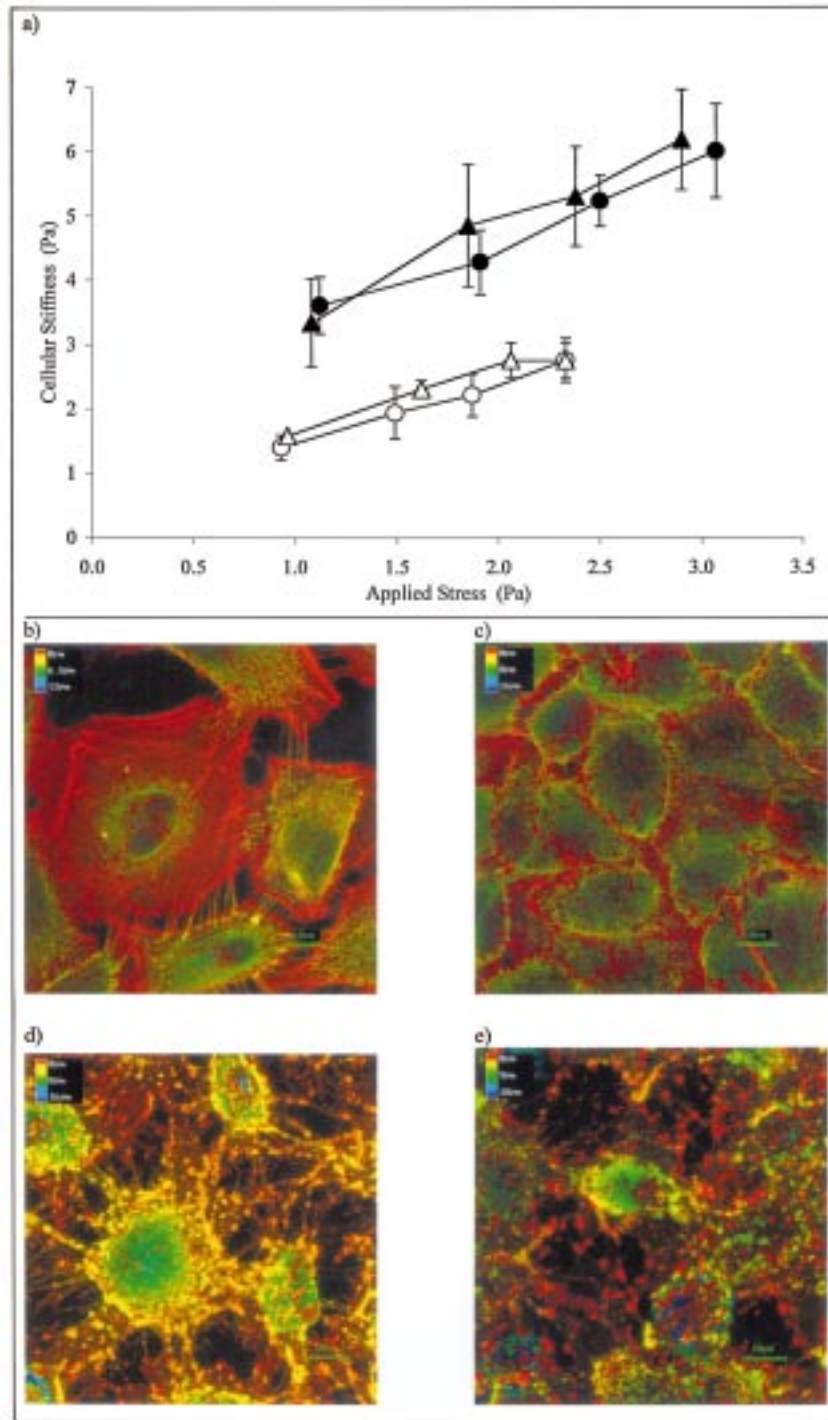


Fig. 5. Cytoskeleton (CSK) stiffness assessed by magnetocytometry (Fig. 5a) and F-actin visualization assessed by confocal microscopy after treatment with fluorescent phallotoxin (Figs. 5b–5e). A549 epithelial cells were plated at a density of 50×10^3 /well or 30×10^3 /well to reach confluence or subconfluence at 24 hours. In Figure 5a, stiffness *versus* applied stress was obtained by magnetocytometry for both confluent (▲) and subconfluent (●) adherent cells before cytochalasin D treatment. Addition of a low concentration of cytochalasin D ($1 \mu\text{g}/\text{ml}$ for 20–30 min) markedly reduced both stiffness and the stiffening response of both confluent (Δ) and subconfluent (○) adherent cells (a). The spatial distribution of actin filaments (presented in Figs. 5b–5e), where actin filaments were colored differently according to their height in the cell, *i.e.*, from red (basal plane: $0 \mu\text{m}$) to dark blue (apical plane: $18 \mu\text{m}$). In (b), staining of the F-actin cytoskeleton in subconfluent cells revealed a high density of F-actin organized into stress fibers in a thin inferior layer shown in red. In Figure 5c, confluent cells appear less spread with a marked contour of F-actin, as spreading is limited by the adjacent cells. In Figures 5d and 5e, partial depolymerization of F-actin fibers and splitting of actin filaments into shorter lengths are visible after cytochalasin D treatment for both subconfluent (Fig. 5d) and confluent cells (Fig. 5e).

implied very small values of persistent (initial) strain for the cables ($\varepsilon = 0.03\%$ or $T^* = 3 \times 10^{-4}$) when buckling of rigid elements was considered in the model [14]. Under these conditions, the strain-stiffening response resembled the stiffening response measured in cultured cells [26].

The cellular scale application conducted by Wendling *et al.* [32] was performed by considering that the rigidity estimated for large degrees of deformation could be considered to reflect a change in the basal state of the structure, *i.e.* the distribution of internal tension in the cables, close to isotropic at small deformations, tends to become increasingly anisotropic as deformation increases. The higher stiffness obtained at large deformation could therefore be attributed to higher degrees of heterogeneity of the cable prestress (Fig. 2). More recently, Stamenovic *et al.* compared the stiffness of spread and round cells by studying the 30-element tensegrity model in two configurations, *i.e.* a “spread” configuration (6 nodes anchored to a rigid substratum) and a “round” configuration (3 anchored nodes) [33]. They showed that the structural stiffness increased with spreading, in line with the observations in cells. Moreover, the predictions of the rigid bar tensegrity model were much closer to the cellular results than predictions based on the buckling bar tensegrity model. Furthermore, the stiffness of the overall structure in Stamenovic’s study was obtained from the ratio of uniaxial force applied to a single superior node and its displacement in the direction of the force applied, which differs from our approach ([32] and present study). It should also be emphasized that the shape of the tensegrity structure anchored at 6 nodes, at the referential state, was asymmetrical due to a heterogeneous tension distribution in the cables [33], while the shape of the structure anchored at 3 nodes was symmetrical, due to homogeneous tension distribution. The various theoretical results obtained on 30-element tensegrity structures and the present experimental results therefore consistently suggest that higher heterogeneity in prestress results in higher structural stiffness. Interestingly, the theoretical results presented in Figures 3 and 4 were obtained with homogeneous prestress, *i.e.* with a symmetrical shape at reference state, but with various predetermined numbers of spatially fixed nodes.

4.2 Tensegrity model to describe cell prestress vs. stiffness

Our study on adherent epithelial cells was performed with a cytochalasin D concentration and incubation time which produced partial F-actin depolymerization with an expected minimal effect on cell shape and cell-ECM attachment. Accordingly, alterations in both stiffness and stiffening response of the cytochalasin D-treated cells resulted from disruption of the actin lattice, which was particularly visible in the basal plane of subconfluent cells (Fig. 5d), whereas this disruption seemed to be less marked at the apical pole of some cells. Although specific staining of other CSK polymeric networks was not performed in this study, the integrity of microtubules and intermediate

filaments was thought to be preserved, as suggested by previous studies [29,30]. The essential effect of cytochalasin D on cytoskeletal inner properties would be a reduction of the cytoskeletal internal tension secondary to rupture of the cytoskeletal lattice continuity [7,26]. Splitting of actin filaments into shorter lengths has been shown to be associated with an increased amount of filamentous actin [34]. In our study, cellular size was roughly maintained even after cytochalasin D treatment (Figs. 5d–5e), probably due to preservation of the integrity of non-actin filaments and, to a certain extent, maintenance of cell-ECM attachments and a persistent veil of microfilaments at the apical pole. This allowed us to maintain a constant characteristic length of the elements in the theoretical model in order to simulate both high and low levels of internal tension. The present results and previous results obtained with the 30-element tensegrity model fully support the assumption that the lower the prestress, the lower the stiffness, when the range of the initial cable strain is limited ($T^* \ll 1$). Various arguments derived from the literature support the idea that T^* values estimated in cells are consistent with this stiffness affected T^* -range. As previously performed by Coughlin and Stamenovic [14], we roughly estimated the biological values of $T^*(= T_c^{(r)}/E_c S_c)$ in the range $[2 \times 10^{-3} - 2 \times 10^{-4}]$ using previously published data, *i.e.* a $[10 - 100 \text{ pN}]$ range for the F-actin pre-stretching force $T_c^{(r)}$ [35–37], a value of 2.6 GPa for Young’s modulus of an isolated actin filament E_c , and a cross-sectional area of 18 nm^2 for the filament [35].

The 30-element tensegrity model can also be used to explain attenuation of the stiffening response measured in cytochalasin D-treated epithelial cells (Fig. 5a). In a recent study by our group [32], we theoretically demonstrated that the strain stiffening response of the tensegrity structure was moderately decreased when the internal tension was decreased by several orders of magnitude. Note that significant changes in T^* values for the physical tensegrity structure tested in this study (Figs. 2b and 2d) consistently resulted in moderate changes in the initial slope of $E_A^* - \varepsilon$ relationships, as well as a moderate change in the curvilinearity of $E_A^* - \varepsilon$ curves. By analogy, cytochalasin D, which is thought to strongly affect the elastic properties of actin filaments, appears to less markedly reduce both stiffness and the stiffening response (Fig. 5) [7,26].

4.3 Tensegrity model to describe cell environment vs. stiffness

It may appear surprising that untreated subconfluent and confluent cells exhibit almost similar stiffness properties from lower to higher values of stress, *i.e.* the stiffening response is not modified, while cell-cell interconnections and cell-ECM attachment conditions probably both differ in response to changes in growth conditions. It therefore seems difficult to evaluate their respective effects on stiffness. The theoretical model is able to mimic the effect of changing cell-cell connections by varying the number of additional spatially fixed nodes without changing the number of nodes anchored to the rigid substratum.

CSK stiffness predicted by the model tended to increase with the number of spatially fixed nodes, indicating that confluent cells would be stiffer than subconfluent cells under identical cell-ECM attachment conditions. The almost equivalent rigidity measured in the two different growth conditions tested led us to assume that cell-ECM attachment was weaker in confluent cells than in the subconfluent cells tested here. This is consistent with the smaller number of F-actin bundles observed in confluent cells compared to subconfluent cells (Figs. 5b and 5c). In a previous study, Wang and Ingber showed that spread endothelial cells (obtained with a high density of ECM-fibronectin) exhibited an increase in both CSK stiffness and stiffening response compared to non-confluent round cells (obtained with a low density of ECM-fibronectin) [6]. This result was predicted by the 30-element tensegrity model of Coughlin and Stamenovic [33], considering the non-isotropic distribution of internal tension at low stress in addition to the increased number of attachment points.

The present study indicates similarities between the 30-element model and adherent cell behaviors, which appear complementary of those previously described [13]. However, we are aware that a number of questions remain unclear. In particular, we do not consider the possibility of biochemical remodeling between confluent and subconfluent cells, or before and after treatment with cytochalasin D. Some of the limitations of the theoretical model are discussed below.

Firstly, analysis of the effects of cytochalasin D was mimicked on the model by assuming that internal tension was modified, while the characteristic length of the structural elements remained the same before and after cytochalasin D treatment. Our assumption supposes that the structure composed of depolymerized actin filaments becomes supported by non-actin filaments, *i.e.* microtubules and intermediate filaments, and by persistence of a veil of actin filaments near the apical pole of certain cells. These cellular effects induced by cytochalasin D treatment would result in a reduction of internal tension, without totally eliminating tensional integrity, as evidenced by the preserved elastic response of treated cells (see Fig. 5a). Indeed, depolymerization of microtubules tends to reduce CSK stiffness, but to a lesser degree than depolymerization of actin filaments, which confirms that microtubules might play a role in the basal state of cytochalasin D-treated cells [26,30]. Moreover, depolymerization of both microtubules and intermediate filaments in addition to actin filaments has been shown to result in complete suppression of rigidity [26].

Secondly, we could have used a higher cytochalasin D concentration (or a longer incubation time) which would have more markedly altered cell-ECM attachment conditions and cell-cell interrelations. We did not study the effect of these conditions, as we wanted to focus on the change in CSK internal tension without changing cell shape. Moreover, it cannot be excluded that, in addition to maintenance of the non-actin CSK networks, the environmental conditions of the studied cell (cell-ECM attachments and cell-cell interrelations) may have

participated in maintenance of the overall size of the cell before and after cytochalasin D treatment. In this study, the environmental conditions specific to confluent cells were taken into account in the model by fixing an increasing number of nodes. We are aware that creating an additional number of fixed nodes in order to represent the interactions with confluent cells constitutes an oversimplification because adjacent cells tend to behave like other deformable tensegrity structures. It should also be emphasized that the 30-element tensegrity model, already oversimplified in comparison with the complex CSK structure, is limited in terms of geometrical mobility when the number of fixed nodes is increased from 3 to 6 or 9, as, in such cases, 50% ($N = 6$) or 75% ($N = 9$) of the nodes are fixed in the tensegrity structure, which is not necessarily representative of the proportion of cell-cell interrelations or cell-ECM attachment conditions observed in cell cultures. Overall, these results show that tensegrity is a useful concept to describe the mechanical behavior of epithelial cells in culture when internal and external factors are modified. Further studies should therefore be conducted to evaluate cellular stiffness in the context of an epithelium, *e.g.* using a hierarchical organized model comprised of elementary tensegrity structures.

We gratefully thank D. Stamenovic (Boston University), J.J. Fredberg and N. Wang (Harvard School of Public Health) for helpful discussions. Study partly supported by INSERM grant No. 4M106C.

References

1. P.F. Davies, A. Robotewskyj, M.L. Griem, *J. Clin. Invest.* **93**, 2031 (1994).
2. D. Ingber, J. Folkman, in *Cell shape: Determinants, Regulation and Regulatory Role* (S. W.D. and B. F., Editors, 1989), pp. 3–31.
3. M.S. Kolodney, E.L. Elson, *Proc. Natl. Acad. Sci. USA* **92**, 10252 (1995).
4. D. Choquet, D.P. Felsenfeld, M.P. Sheetz, *Cell* **88**, 39 (1997).
5. E. Planus *et al.*, *J. Cell Sci.* **112**, 243 (1998).
6. N. Wang, D.E. Ingber, *Biophys. J.* **66**, 1 (1994).
7. J. Pourati *et al.*, *Am. J. Physiol.* **272**, C1283 (1998).
8. S.R. Heidemann, *Science* **260**, 1080 (1993).
9. *Cellular Solids, Structure and Properties*, edited by L.J. Gibson, M.F. Ashby (Pergamon Press, 1988).
10. *Biomechanics; Mechanical properties of living tissues*, edited by Y.C. Fung (Springer Verlag, 1981), Vol. 1.
11. E. Evans, A. Yeung, *Biophys. J.* **56**, 151 (1989).
12. R.M. Hochmuth, R.E. Waugh, *Annu. Rev. Physiol.* **49**, 209 (1987).
13. D. Stamenovic *et al.*, *J. Theor. Biol.* **181**, 125 (1996).
14. M.F. Coughlin, D. Stamenovic, *J. Appl. Mech.* **64**, 480 (1997).
15. *Introduction to tensegrity*, edited by A. Pugh (University of California Press, 1976).
16. D.E. Ingber, J.D. Jamieson, in *Gene expression during normal and malignant differentiation*, edited by L. Anderson, C. Gahmberg, P. Ekblom (San Diego Academic Press, 1985), pp. 13–32.

17. A.J. Maniotis, C.S. Chen, D.E. Ingber, Proc. Natl. Acad. Sci. USA **94**, 849 (1997).
18. T.J. Dennerll, R.E. Buxbaum, S.R. Heidemann, J. Cell Biol. **107**, 665 (1988).
19. B. Danowski, J. Cell Sci. **93**, 255 (1989).
20. A.K. Harris, P. Wild, D. Stopak, Science **208**, 177 (1980).
21. *Geodesic Math and How to Use It*, edited by H. Kenner (University of California Press, 1976).
22. F. Mohri, R. Motro, Struct. Eng. Rev. **5**, 231 (1993).
23. J.H. Argyris, D.W. Scharpf, J. Struct. Div. **106**, 633 (1972).
24. V. Laurent *et al.*, Arch. Physiol. Biochem. **106**, 183 (1998).
25. N. Wang, D. Ingber, P. Butler, Focus **3**, 3 (1993).
26. N. Wang, J. Butler, D. Ingber, Science **260**, 1124 (1993).
27. D.E. Ingber, S. Karp, J. Cell Biol. **115**, 394A (1991).
28. N. Wang, D.E. Ingber, Biochem. Cell Biol. **73**, 1 (1995).
29. M. Schliwa, J.V. Blerkom, J. Cell Biol. **90**, 222 (1981).
30. U.S.B. Potard, J.P. Butler, N. Wang, Am. J. Physiol. **272**, C1654 (1997).
31. O. Thoumine *et al.*, Exp. Cell Res. **219**, 427 (1995).
32. S. Wendling, C. Oddou, D. Isabey, J. Theor. Biol. **196**, 309 (1999).
33. M.F. Coughlin, D. Stamenovic, J. Biomech. Eng. **120**, 770 (1998).
34. H.P. Ting-Beall, A.S. Lee, R.M. Hochmuth, Ann. Biomed. Eng. **23**, 666 (1995).
35. F. Gittes *et al.*, J. Cell Biol. **120**, 923 (1993).
36. H. Kojima, A. Ishijima, T. Yanagida, Proc. Natl. Acad. Sci. USA **91**, 12962 (1994).
37. O. Thoumine, J. Phys. III France **6**, 1555 (1996).

Nomenclature

Laboratory abbreviations

BSA:	Bovine Serum Albumin
CO ₂ :	Carbon dioxide
CSK:	Cytoskeleton
Cyto D:	Cytochalasin D
ddH ₂ O:	Double distilled water
DMEM:	Dulbecco Modified Eagle's Medium
ECM:	Extracellular matrix
EDTA:	Ethylene-Diamine-Tetra-Acetic acid
EGTA:	Ethylene-Glycol-Tetra-Acetic acid
FBS:	Fetal Bovine Serum
HEPES:	4-(2-hydroxyethyl)-1-piperazineethanesulfonic acid (biological buffer)
MES:	2-(N-morpholino)-ethanesulfonic acid (biological buffer)
MgCl ₂ :	Magnesium chloride
MTC:	Magnetocytometry
PBS:	Phosphate Buffer Saline
RGD:	Arginine-glycine-aspartic acid
1 mM =	10 ⁻³ mole

Mechanical abbreviations

T_c :	pre-stretching force
$T_c^{(r)}$:	pre-stretching force at reference state
T_b :	pre-compressing force
T_p :	pre-stressing force of a given element
l_c :	tensile element (elastic cable) length
l_{0p} :	resting length of a given element
$l_c^{(r)}$:	elastic element (cable) length at reference state
l_b :	compressive element (bar) length
S_c :	elastic element cross-sectional area taken to be invariable
S_b :	compressive element cross-sectional area taken to be invariant
r_c :	elastic element radius taken to be invariant
E_p :	Young's modulus of a given element
E_b :	invariable Young's Modulus of the bar
E_c :	invariable Young's Modulus of the cable
$(E_c S_c)$:	elastic recoil force of the cable or product of Young's modulus of the cable and the cross-sectional area
$(E_b S_b)$:	elastic recoil force of the bar or product of Young's modulus of the bar and the cross-sectional area
$\{\mathbf{F}\}$:	column vector of external forces applied to the overall structure (dimensions: $[1 \times 36]$)
$\{\mathbf{u}\}$:	column vector of nodal displacements of the overall structure (dimensions: $[1 \times 36]$)
$[\mathbf{K}]$:	global rigidity hypermatrix of the overall structure (dimensions: $[36 \times 36]$)
$[\mathbf{K}]_p$:	global rigidity matrix of a given element (dimensions: $[3 \times 3]$)
$[\mathbf{K}_E]_p$:	elastic rigidity matrix of a given element (dimension $[3 \times 3]$)
$[\mathbf{K}_G]_p$:	geometrical rigidity matrix of a given element (dimension $[3 \times 3]$)
$(c_x; c_y; c_z)_p$:	director cosines vector of a given element
$(x_i; x_j)$:	the x -axis coordinates of nodal points (i, j)
S_0 :	equivalent section of the tensegrity structure
L_0 :	equivalent length of the tensegrity structure
ΔL_k :	relative displacement along the k -axis
ε :	strain or deformation of the tensegrity structure
σ :	stress of the tensegrity structure
E_A :	apparent elasticity modulus of the structure
E_A^* :	normalized elasticity modulus of the structure
L^* :	normalized elastic element length
T^* :	normalized elastic tension
1 pN =	10 ⁻¹² N (Newton)
1 nm =	10 ⁻⁹ m (meter)
1 Pa =	1 Pascal; pressure unit
1 MPa =	10 ⁶ N/m ²